VEHICLE SPEED DETERMINATION WITH INDUCTIVE-LOOP TECHNOLOGY AND FAST AND ACCURATE FRACTIONAL TIME DELAY ESTIMATION BY DFT

Krzysztof Duda, Zbigniew Marszalek

AGH University of Krakow, Faculty of Electrical Engineering, Automatics, Computer Science and Biomedical Engineering, Department of Measurement and Electronics, al. Mickiewicza 30, 30-059 Kraków, Poland (✉ *kduda@agh.edu.pl*)

Abstract

Inductive loop (IL) sensors, which are permanently installed in the road, output signals for the evaluation of vehicle magnetic profiles (VMPs) as vehicles pass over them. VMPs are acquired using a multi-frequency impedance measurement (MFIM) system equipped with advanced electronic, signal processing, and data management capabilities. The vehicle speed is calculated by measuring the time shift (delay, lag) between VMPs obtained from two distant IL sensors. The cross-correlation sequence (CCS) estimate is a widely accepted method for estimating time shifts that are integer multiples of the sampling period, *i.e.*, the time resolution of the CCS is limited by the sampling period. In this paper, we present a fully operational MFIM system equipped with two wide and two slim IL sensors. We apply the Discrete Fourier Transform (DFT) to estimate fractional time shifts, *i.e.* we obtain a time resolution higher than the sampling period. Field measurement signals demonstrate that the proposed application of the DFT for fractional shift estimation offers higher accuracy, lower computational complexity, and better noise immunity compared to the CCS-based estimation. For short-duration signals, the DFT-based shift estimation is unbiased, while the CCS is a biased time shift estimator.

Keywords: cross-correlation sequence, discrete Fourier Transform, fractional delay FIR filter, fractional shift estimation, inductive loop, multi-frequency impedance measurement, time shift, vehicle magnetic profile.

1. Introduction

In this paper, we present a *multi-frequency impedance measurement* (MFIM) system equipped with inductive-loop technology [1-3] and describe a vehicle speed computation algorithm based on the DFT fractional shift estimation that outperforms the widely used *cross-correlation* (CC) method.

The inductive-loop technology has gained significant popularity in road traffic measurements [1-8]. A recorded *vehicle magnetic profile* (VMP) [1] is used for various applications, such as speed and axle-to-axle distance measurement [2], load estimation [3], and advanced vehicle classification using machine learning [4, 5], and neural networks [6, 7]. Road traffic measurement systems also utilize anisotropic magneto-resistive sensors, *e.g.* [9-14]. However, regardless of the type of sensor used, the speed is calculated based on the estimated time shift between two signals. The speed is further used to determine various parameters such as the axle-to-axle distance or vehicle length, which are key inputs for classification algorithms [5, 15, 16]. Estimated speed and vehicle class are also utilized in free-flow traffic models for planned infrastructure development [17].

Therefore, the time shift is a fundamental measurement in road traffic measurement systems.

Time delay estimation is a basic problem in signal processing, *e.g.* [18, 19] with a wide range of applications including traffic measurements and others [11, 14, 20-29]. The main difficulty in road measurement applications is the impulse-like nature of the signals of interest, which are of short duration, making reliable correlation estimates practically unattainable. For instance,

techniques such as segment averaging [19] are not applicable. The VMPs analyzed in this paper contain approximately one oscillation, similar to the magnetic field readings in [9], while the magnetic field signals analyzed in [11] have around three oscillations.

For correlation-based shift estimation, an insufficiently high sampling frequency limits the resolution [20-22], and the positioning of the maximum can be problematic for noisy signals and flat cross-correlation functions. Some remedies to improve the performance of the correlation include: various interpolation techniques, such as parabolic fit [23], normalized cross-correlation [24], weighted cross-correlation [25], modified cross-correlation functions [26], and a combination of state-machine detection and cross-correlation detection [27].

The comprehensive investigation of several shift estimation methods conducted in [11] confirmed that the CC method for speed evaluation is the most accurate in road traffic measurements, but at the expense of high computational complexity. The CC resolution of the time shift estimation is limited to the sampling period; therefore, high sampling rates are necessary for high accuracy. The CC can be efficiently computed using the *Fast Fourier Transform* (FFT) algorithm, *e.g.*, [9], however, the measurement signals still need to be heavily oversampled to achieve good time resolution.

In general, the low-oscillation and short-duration nature of VMPs introduce bias in the CC-based shift estimation. We utilize the *Discrete Fourier Transform* (DFT) for fractional shift estimation and not as an algorithm for fast CC computation. We demonstrate that only a few highest magnitude DFT bins are sufficient for fractional shift estimation, and thus the FFT algorithm, that computes all DFT bins, is not used. For the considered VMPs, the DFT is more accurate and simpler to compute than the CC. The proposed DFT-based shift estimation has the following advantages over the existing standard CC-based approach: 1) improved time resolution up to the fraction of a sampling period, 2) unbiased shift estimation for low-oscillation signals, and 3) easy rejection of bandpass disturbances in the frequency domain. Thanks to fractional time resolution, reduced sampling frequencies can be used in the MFIM system. This results in reduced hardware requirements for data management, such as slower ADCs (*Analog-to-Digital Converter*), and also decreases the consumption of computational power.

The paper is organized as follows: Section 2 briefly introduces the MFIM system for the VMP assessment. Section 3 presents the theoretical framework for speed computation, including the definition of the signal model, descriptions of the CC and the DFT algorithms, and the fractional FIR filter used to undo the estimated shift in field signals and to generate artificial test signals. The Results section highlights the advantages of the DFT over the CC for shift estimation. The final section concludes the paper.

2. Vehicle magnetic profile

The developed MFIM system for VMP acquisition [1-3] is depicted in Fig. 1. For a single IL sensor it operates as follows. An impedance is measured, by definition, as the ratio of complex voltage to complex current. However, a voltage excitation source contains a sum of three sinusoidal waves with different frequencies. The complex voltages and currents are obtained from the outputs of quadrature demodulators. A transimpedance amplifier is used to convert a current signal into voltage. The voltages are converted to digital form using a sampling frequency of 400 kHz and a resolution of 16 bits. Demodulation is carried out in software, simultaneously for all three excitation frequencies, using perfectly flat-top filters [1, 30] to prevent amplitude errors. The bandwidth of the filters is chosen to maintain the necessary dynamics of the current and voltage signals for road speeds up to 150 km/h. Finally, the VMPs are downsampled to a 1 kHz sampling frequency.

The developed MFIM system was operating on the internal road at AGH University of Krakow. Figure 2 shows exemplary VMP field recordings captured simultaneously by two processing channels for IL1 and IL3 sensors. R-VMPs represent the real part of the impedance of the IL sensor, while X-VMPs represent the imaginary component of the impedance. Each vehicle induces changes in both impedance components. The real component is often omitted in the literature on IL sensors due to its generally lower value. VMPs obtained at a low frequency (black) exhibit a low amplitude, while at a higher frequency, they demonstrate a higher amplitude (red). Due to the 1.5 m distance between IL1 and IL3, we observe VMP sequences that are shifted in time.
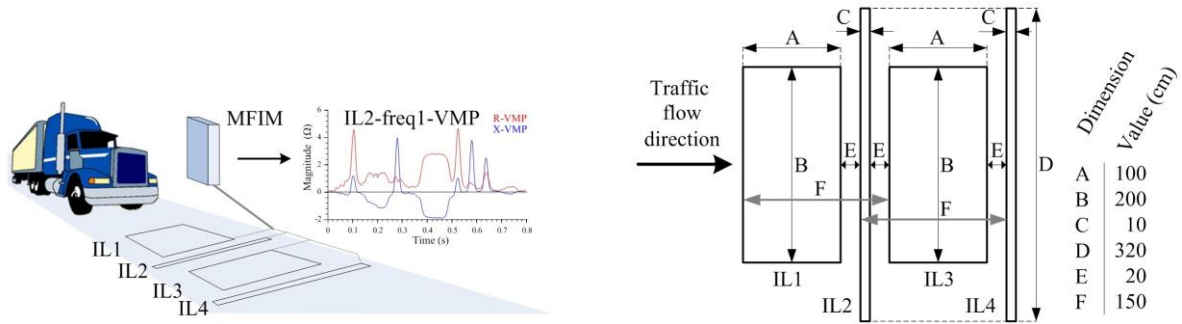

Fig. 1. MFIM system for VMP recording (left), IL sensors layout with dimensions (right).
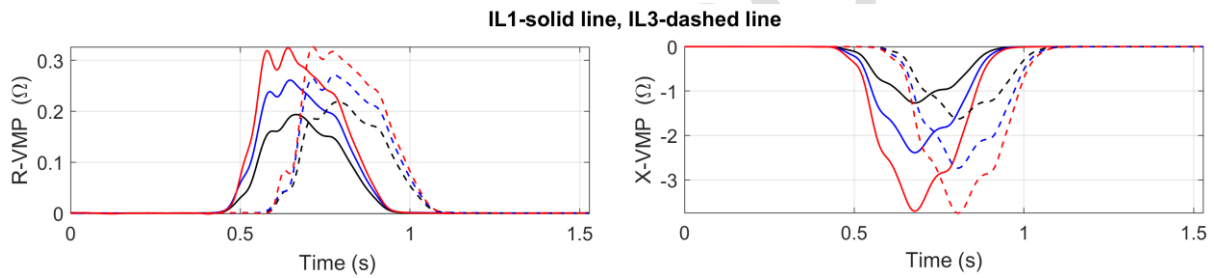

Fig. 2. Exemplary VMPs recorded by IL1 and IL3. R-VMP–resistance (left), X-VMP–reactance (right). Excitation frequency is the lowest, the middle and the highest for black, blue and red line, respectively.
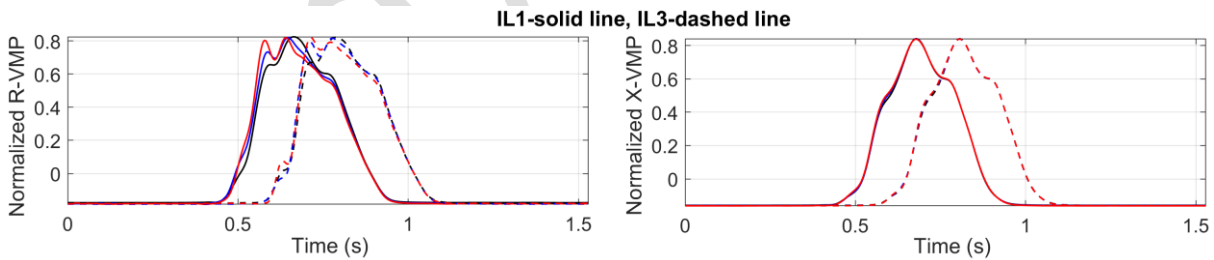
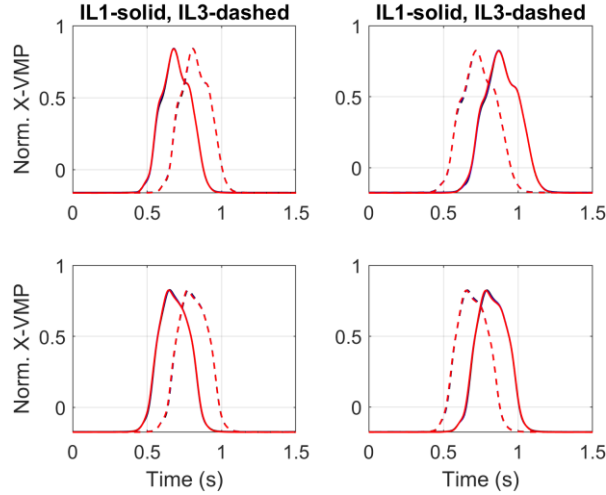

Fig. 3. Normalized VMPs from Fig. 2.

Fig. 4. Normalized X-VMPs for two cars driving in two directions: Mercedes GLA200 (upper row), Hyundai ix35 (bottom row). Direction from IL1 to IL3 (left column), direction from IL3 to IL1 (right column).

The VMPs are measured simultaneously on three frequencies for increasing the robustness against *electromagnetic interference* (EMI) that has a bandpass frequency spectrum, and rarely strongly affects all three excitations at ones. In the absence of the EMI all three VMPs are very similar in shape, especially |X-VMP|, and after normalization they overlap, as shown in Figs. 3, 4. The normalized R-VMPs overlap less than the X-VMPs. Further, to determine the vehicle speed, X-VMPs are used. Figure 4 shows the normalized X-VMP for two passenger cars moving in two directions, which results in a different order of the X-VMP sequences in time. The VMPs depicted in Fig. 4 are representative of the entire class of VMP signals measured in our MFIM system and are therefore used as test signals in the Results section.

3. Time delay estimation

3.1. Signal model

Ideally, the discrete-time VMP acquired by the IL1 sensor, see Fig. 1, and denoted by $p_1[n]$, should be a delayed version of VMP $p_3[n]$ recorded by the IL3 sensor. However, due to real-world imperfections, this relationship is more complicated. Both VMPs are observed in the presence of slightly different additive disturbances. The gain in both channels is not exactly the same, and the shapes of both VMPs are also slightly different. We assume the following relation between the two VMPs

$$p_1[n] = ap_3[n - n_s] + \varepsilon[n], \tag{1}$$

where $n=0,1,\ldots,N$-1 and N is the number of samples, $a>0$ is a gain coefficient (in the considered application, close to 1 thanks to signal normalization before shift estimation, see Fig. 4), $\varepsilon[n]$ is a disturbance representing measurement noise of both VMPs and shape inconsistencies between them, and finally n_s is a shift to be estimated that can be integer or fractional.

3.2. CCS-based time delay estimation

The integer part of the shift n_s can be estimated by finding the maximum of the *cross-correlation sequence* (CCS) estimate defined, between two arbitrary length N signals $x[n]$ and $y[n]$, by

$$R_{xy}[m] = \sum_{n=0}^{N-m-1} x[n + m]y[n], \tag{2}$$

with $m=-(N-1),\ldots,-1,0,1,\ldots,N-1$. Then

$$round(n_s) = m_{max}, \tag{3}$$

where m_{max} is a shift (lag) for the maximum value of the CCS between VMPs $p_1[n]$ and $p_3[n]$. The time resolution of the CCS-based shift estimation (3) is limited to the length of the sampling period as indicated by the rounding off function in (3).

Figure 5 (left) depicts the CCS estimate (2) between $p_3[n]$ and $p_1[n]$ for normalized X-VMPs in Fig. 4 (Mercedes GLA200, direction from IL3 to IL1, middle frequency). For this case the highest difference between the CCS-based, and DFT-based shift estimation is observed. In the considered application, see Fig. 1, time delay has always known sign, thus it is sufficient to apply (2) either only for $m>0$ or for $m<0$.

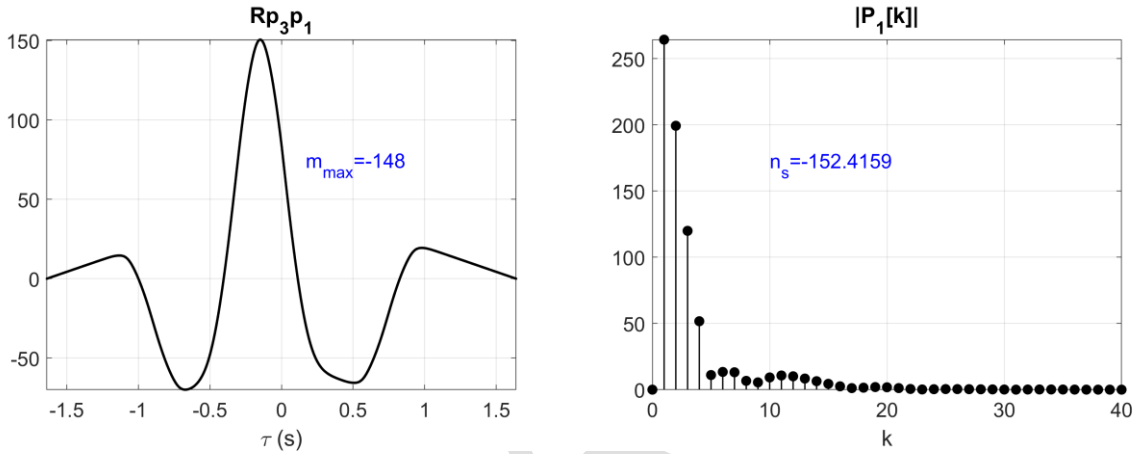Fig. 5. The CCS estimate (2) between $p_3[n]$ and $p_1[n]$ (left), see Fig. 4, and the fragment of the magnitude DFT of $p_1[n]$ (4) (right).

3.3. DFT-based time delay estimation

The DFT $X[k]$ of an arbitrary length N signal $x[n]$ is defined as [14]

$$X[k] = \sum_{n=0}^{N-1} x[n]e^{-j\frac{2\pi}{N}kn}, \tag{4}$$

and $k=0,1,\ldots,N-1$. The DFT has the property of circular shift of the sequence [14]. Let us assume that $p_1[n]$ is a circularly delated version of $p_3[n]$, as denoted by tilde in (5)

$$\widetilde{p_1}[n] = \widetilde{p_3}[n - n_s], \tag{5}$$

then the DFT spectra of $p_1[n]$ and $p_3[n]$ denoted by $P_1[k]$ and $P_3[k]$ obey the following relation

$$P_1[k] = e^{-j\frac{2\pi}{N}kn_s}P_3[k]. \tag{6}$$

The delay is estimated as

$$n_s^k = -\frac{N}{2\pi k} angle\big(P_1[k]\text{conj}(P_3[k])\big), k \neq 0, \tag{7}$$

where the function *angle( )* returns the phase angle of a complex number, and k denotes the DFT bin selected for estimation. In (7) we prefer to use multiplication instead of division, *i.e.* $angle(P_1[k]/(P_3[k]))$, because division is more susceptible to disturbances, especially when the denominator is small.

Fig. 5 (right) depicts the fragment of the magnitude DFT spectrum of $p_1[n]$. It is observed that the DC component is completely removed by subtracting the mean value in the time domain, and that the DFT bin with $k=1$ has the highest magnitude. For a considered class of

VMP signals the DFT bin with $k=1$ is always the highest one and it is the first choice to be used in (7). However, bins $k=2$ and $k=3$ are also valid to be used in (7). The delay can also be estimated by a combination of several n_s^k, *e.g.* the mean value

$$n_s^{1,2} = \frac{n_s^1 + n_s^2}{2}, \tag{8}$$

$$n_s^{1,2,3} = \frac{n_s^1 + n_s^2 + n_s^3}{3}. \tag{9}$$

In case of disturbance with a similar power spread in DFT bins $k=1,2,3$ the bin with the highest magnitude has the highest signal to noise ratio. The DFT bins with higher indices must not be used in (7) as they are caused by the spectral leakage.

The delay estimated by (7) may be fractional, thus the time resolution is not limited by the sampling period length, as it is in the case of the CCS-based estimation (3). According to (7) it is enough to compute only 2 DFT bins for delay estimation, but (8) and (9) require 4 and 6 DFT bins, respectively.

3.4. Fractional delay FIR filter

The fractional delay FIR filter is used in the next section to compensate for the estimated shift in order to evaluate the quality of shift estimation and to generate test signals with known shift.

Equation (6) expresses a filtration in the frequency domain, *i.e.* $P_1(\omega) = H(\omega)P_3(\omega)$, where ω denotes the frequency in radians. Theoretical impulse response $h[n]$ of an ideal delay filter $H(\omega) = e^{-j\omega n_s}$ is computed by the inverse discrete time Fourier transform (DTFT) [31]

$$h[n] = \frac{1}{2\pi} \int_{-\pi}^{\pi} e^{-j\omega n_s} e^{j\omega n} d\omega = \begin{cases} \frac{\sin(\pi(n-n_s))}{\pi(n-n_s)}, & n - n_s \neq 0 \\ 1, & n - n_s = 0 \end{cases}. \tag{10}$$

The finite impulse response (FIR) filter can be designed by (10) by the window method [31].

Figure 6 depicts an impulse response of a delay filter designed with the rectangular window for $n_s=152.4159$ sampling times, *i.e.* the case in Fig. 5 (right). The impulse response has 501 coefficients. The frequency response of the FIR filter designed with the rectangular, the Hann, the Hamming and the Blackman window is presented in Fig. 7. Figure 7 (left) depicts the magnitude error, and Fig. 7 (right) depicts the shift introduced by the filter. It is observed that the filter with the Blackman window has the highest accuracy in this comparison, and thus it is further used in the section Results.

The selected time window determines the frequency response of the designed filter. The rectangular window has the highest sidelobes and the narrowest main lobe, resulting in the filter having the highest ripples in the frequency response and the narrowest transition band near the frequency of π radians. All other windows have better attenuation of the sidelobes, which translates to reduced ripples in the frequency response. It is observed in Fig. 7 that the frequency response of the filter using the Blackman window is practically flat. However, windows with even higher attenuation of the sidelobes, see *e.g.* [31, 32], can also be used, as well as other existing methods for fractional delay filter design, *e.g.* [33].
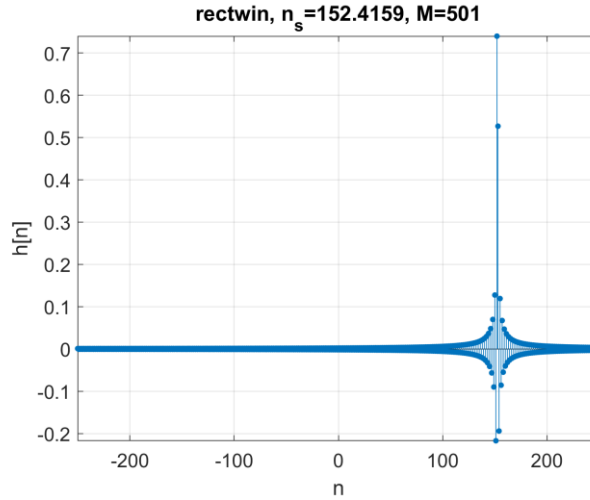
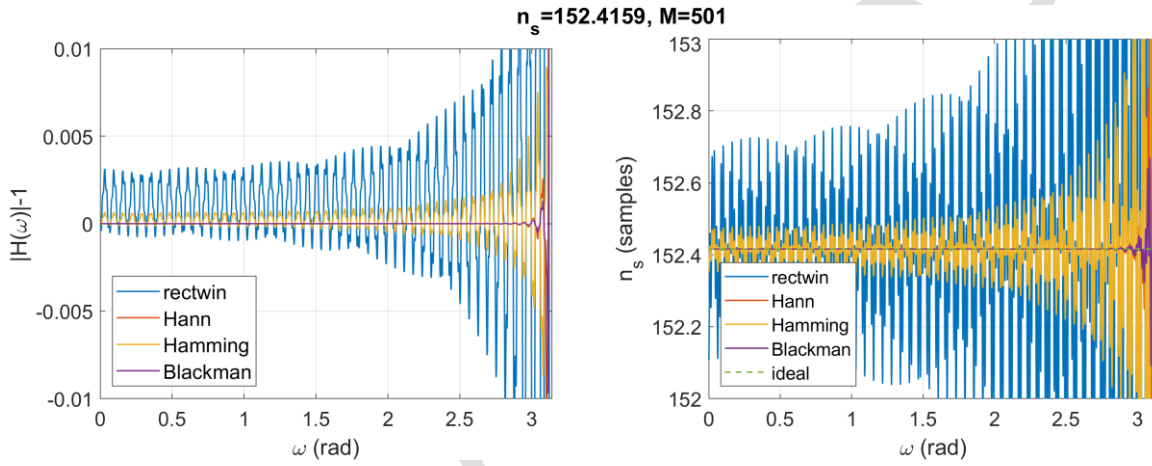Fig. 6. The impulse response of a delay filter designed with the rectangular window for n_s=152.4159.

Fig. 7. Magnitude error (left) and the delay (right) of the FIR filter designed with different windows (see legend). Results for the Hamming window overlap the results for the Hann window.

4. Results

In this section, we illustrate the capability of the proposed DFT-based algorithm for estimating fractional time delays and compare the results with the CCS-based approach. The presented results were obtained using a real-world signals recorder by the MFIM system described in Section II. Figure 4 shows field measurements of the exploited VMPs $p_1[n]$ and $p_3[n]$ obtained in the designed MFIM system. All VMPs are initially preprocessed, *i.e.*, prepared for delay estimation. Preprocessing involves downsampling to 1 kHz, amplitude normalization, and removing the mean value. It is observed that VMPs are similar to each other, but not identical. Acquired VMPs are pulse-like signals, *i.e.*, they do not oscillate.

4.1. Implementational considerations

Figure 5 (left) shows the CCS estimate (2) between $p_3[n]$ and $p_1[n]$. The maximum CCS occurs at m_{max}=-148, resulting in a time delay of -148 ms and a speed of 10.14 m/s (36.49 km/h). If we assume that the CCS has a smooth global maximum and the driving direction is known, the following procedure can be used to find this maximum. Start by computing three successive values of CCS for the most frequently observed speed in the MFIM system, *e.g.* 35 km/h. If the middle value is the highest, then it is a searched global maximum. Otherwise, if the CCS

sequence is increasing in value, compute the next value of the CCS until the first decreasing value is reached. The global maximum is the value calculated prior to the last value. If the CCS sequence is decreasing, then search for the maximum by computing the previous values. The above procedure requires the computation of at least three values of CCS, and the final number of computed CCS values depends on the assumed initial speed (time delay) and the measured speed (delay). Still, there is no need to calculate all values of the CCS estimate, as shown in Fig. 5 (left) for the purpose of illustration.

Fig. 5 (right) depicts the beginning fragment of the magnitude DFT of $p_1[n]$ (4). In the considered MFIM system, VMPs contain approximately one oscillation, *i.e.*, the DFT bin $k=1$ has the highest magnitude. For the considered class of signals it is sufficient to compute only 2 DFT bins for shift estimation according to (7). This is a significant advantage over the CCS-based shift estimation, as the computational load for the DFT-based estimation is fixed and often lower than that for the CCS. In this example, the estimated shift is fractional, with n_s=-152.4159, and the corresponding speed is 9.84 m/s (35.43 km/h). The DFT has an advantage over the CCS in that it can estimate fractional shifts, *i.e.*, shifts occurring between sampling times, whereas the result in CCS is quantized to sampling instances. We can leverage this property of the DFT by additionally downsampling the VMPs Q times prior to shift estimation, as illustrated in the following subsection.

The computational complexity of the CCS (2) for all lags m, is proportional to N^2 operations but can be reduced to $N\log_2 N$ operations by applying the FFT algorithm [8]. However, we only need to find the maximum of CCS, and thus typically a reduced number of M CCS coefficients must be evaluated, with $3 \leq M \ll 2N$. The computation of a single CCS coefficient has complexity proportional to N. However, for high time resolution, the sampling frequency must be high, and thus the number of samples N in VMP must also be high.

The computation of a single DFT bin requires N operations. By employing DFT-based fractional shift estimation (7-9) a high time resolution is maintained even when VMPs are downsampled by a factor of Q. Thus, the proposed DFT-based method is $MN/(2N/Q)=MQ/2$ times faster than the CCS.

4.2. Field test signals

Tab. 1 and Tab. 2 present the results of shift and speed estimation for all signals depicted in Fig. 4, using the CCS and the DFT, respectively. There are some inconsistencies observed between the two methods. The case of the highest and the lowest absolute difference in shift estimation between the CCS-based and the DFT-based algorithms is marked in red and green, respectively, in Tab. 1 and Tab. 2. The values of differences are 4.41 and 1.75.

The quality of shift estimation can be assessed by the effectiveness of VMPs adjustment following shift compensation. Figure 8 depicts the absolute difference between the VMP $p_1[n]$ and $p_3[n]$ adjusted according to the shift as estimated by the CCS and DFT. The shift was compensated for by using a fractional delay FIR filter with the Blackman window, as shown in Fig. 7. It is observed that a better adjustment is obtained for the shift estimation based on the DFT. The quantitative comparison is based on the maximum value of the absolute difference and the *root mean square* (RMS) value of the absolute difference, both of which are provided in the legend.

Figure 9 depicts the maximum and RMS values of the absolute difference between the VMP $p_1[n]$ and $p_3[n]$, adjusted based on the shift as estimated by the CCS and the DFT for all measured signals. VMPs were adjusted by the fractional delay FIR filter designed with the Blackman window shown in Fig. 7. The measurement number refers to the signals in Tab. 1 and Tab. 2 column-wise. The DFT-based shift estimation outperforms the CCS-based estimation for all test signals considered. The error in the delay estimated from the DFT bins

$k=1$, $k=2$, $k=3$ according to (7), (8), (9) is very similar, as it is mainly caused by shape inconsistencies between VMPs $p_1[n]$ and $p_3[n]$ obtained by different IL sensors.

Table 1. CCS-based shift and speed estimation.

	Mercedes GLA200		Hyundai ix35	
	forward	backward	forward	backward
shift (samples)	124	-149	124	-128
	124	-148	124	-128
	125	-147	123	-128
mean shift	124.33	-148	123.67	-128
speed (m/s)	12.1	-10.07	12.1	-11.72
	12.1	-10.13	12.1	-11.72
	12	-10.20	12.2	-11.72
mean speed	12.06	-10.13	12.13	-11.72

Table 2. DFT-based shift and speed estimation.

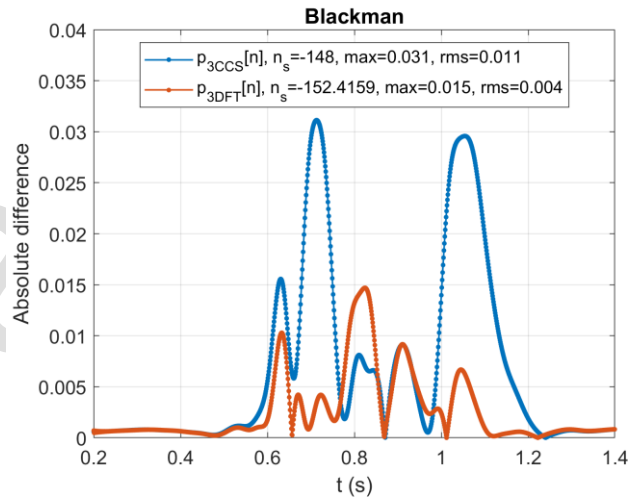|	Mercedes GLA200		Hyundai ix35	
	forward	backward	forward	backward
shift (samples)	126.63	-152.48	125.75	-130.1
	126.47	-152.41	125.83	-130.02
	126.99	-151.39	125.64	-130
mean shift	126.7	-152.1	125.74	-130.04
speed (m/s)	11.85	-9.84	11.93	-11.53
	11.86	-9.84	11.92	-11.54
	11.81	-9.91	11.94	-11.54
mean speed	11.84	-9.86	11.93	-11.53

Fig. 8. The absolute difference between the VMP $p_1[n]$ and $p_3[n]$ adjusted according the shift as estimated by the CCS (blue) and the DFT (red) for $k=1$.
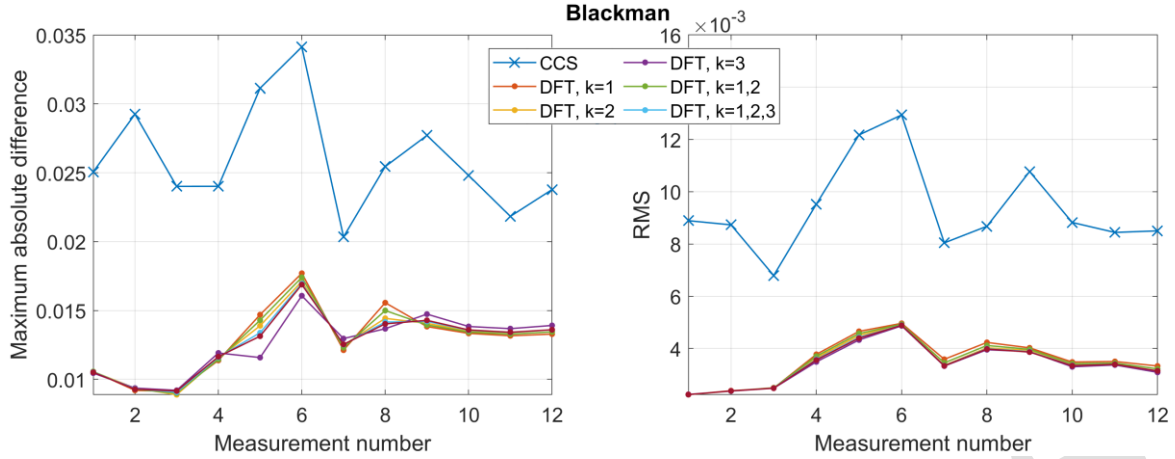
Fig. 9. Maximum and RMS values of the absolute difference between the VMP $p_1[n]$ and $p_3[n]$ adjusted according to the shift as estimated by the CCS and the DFT for all measured signals. In the legend k denotes the DFT bins used for delay estimation based on (7), (8), (9).

4.3. Fractional time delay estimation

Figure 10 shows the test signals used for estimating fractional time delay. The VMP $p_1[n]$, plotted in red, was shifted by the fractional delay FIR filter in the range of n_s from 130 to 170 with an increment of 0.01 sampling period to obtain the set of 4001 test signals plotted in green. In this setup, both VMPs, *i.e.* the red one and the green one, have the same shape.

Figure. 11 depicts the estimation error, which is the difference between the estimated and the true values, obtained for the test signals shown in Fig. 10. It is observed that the estimation based on the DFT is practically unbiased and has a low standard deviation (std). In contrast, the estimation based on the CCS has a significantly higher std due to the requirement for the shift to be an integer value. Additionally, the CCS-based estimation is biased, as indicated by the mean value of an error. The CCS (2) is computed from the overlapping parts of the signals, and for impulse-like signals, such as VMPs, the position of the CCS maximum may be biased. For example, in the case of a shift of $n_s=150$ samples for the signals in Fig. 10, the maximum CCS value of 151.12 is observed at $n_s=146$, while the CCS value for the true shift of $n_s=150$ is only slightly lower and equals 151.07. In the case of the proposed DFT-based estimation, the best results are obtained for a delay computed by (8), *i.e.*, as a mean value of delays estimated based on DFT bins $k=1$ and $k=2$. The worst DFT-based estimator is the one using the DFT bin $k=3$.
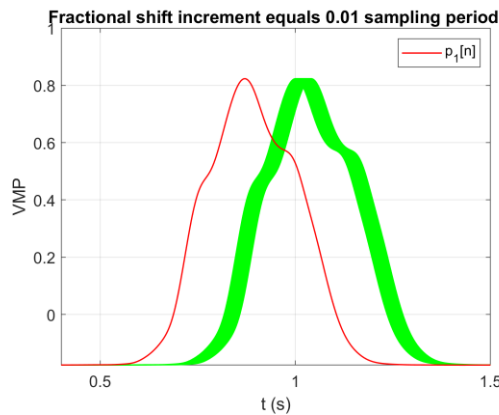

Fig. 10. 4001 test signals (plotted in green) for fractional time delay estimation with 0.01 sampling period increment.
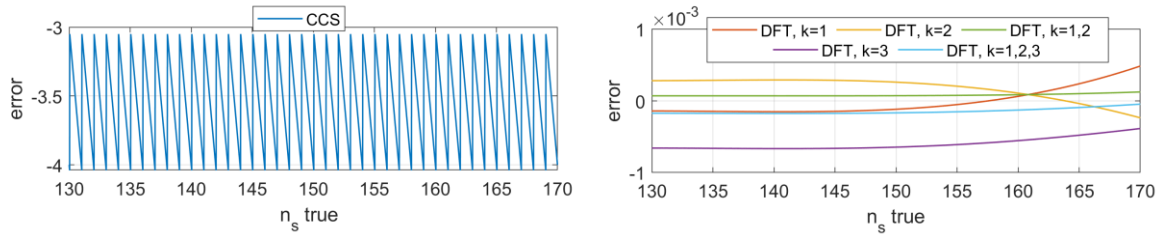
Fig. 11. Fractional shift estimation errors for CCS-based (left) and DFT-based (right) algorithms. The shift is incremented in 0.01 steps, as shown in Fig. 10. The error is the difference between the estimated and true values.
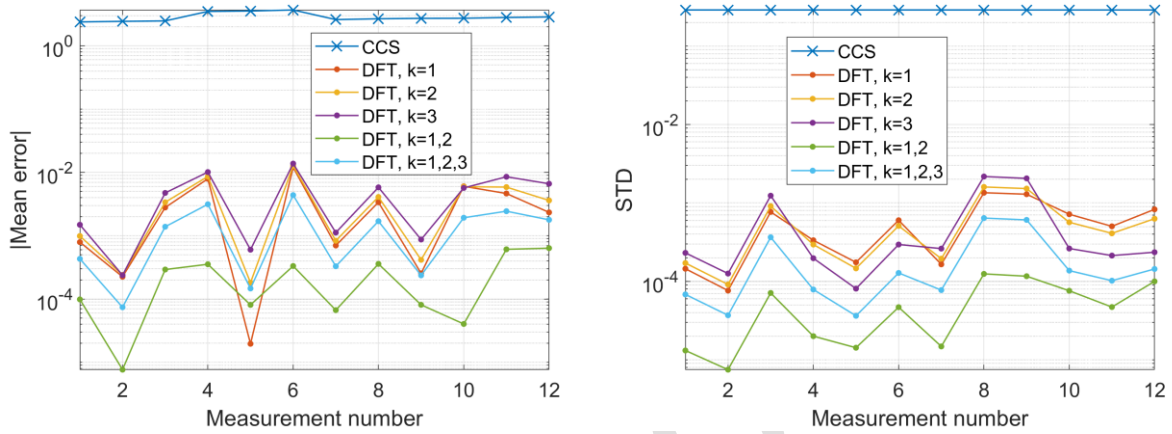

Fig. 12. Absolute mean value and std of fractional shift estimation error for CCS-based and DFT-based algorithms for all measured signals. The shift is incremented with the 0.01 step, see Fig. 10.

The results presented in Figs. 10, 11 were obtained for all 12 test signal shown in Fig. 4. Figure 12 presents the bias and variance of shift estimation by the CCS and the DFT. It has been observed that for a considered class of signals, the estimation based on the DFT is practically unbiased with a negligible std. In contrast, the estimation based on the CCS is biased, at a level of approximately 3 sampling times, with a std of approximately 0.29 sampling times. The best results were once again obtained for the delay calculated using (8).

4.4. Downsampled VMP time delay estimation

Accurate fractional shift estimation of the DFT–based algorithm can be utilized to reduce computational complexity by decreasing the number of samples in VMP through signal downsampling. Figure 13 shows VMPs $p_1[n]$ and $p_3[n]$ at the original sampling frequency F_s, as well as at reduced sampling frequencies $F_s/4$, $F_s/8$, and $F_s/16$. The results of time delay estimation based on downsampled signals are presented in Fig. 14. It is observed that at the original sampling frequency, *i.e.* for $Q=1$, the results for both algorithms are similar. However, with a reduced number of VMP samples, the results for the CCS–based estimation may deviate significantly, whereas for the DFT-based estimation, the results are consistent. For example, it is observed in Fig. 14, that even with $Q=20$, the result for the DFT–based estimation is close to the one obtained with original sampling, *i.e.*, $Q=1$.

Downsampling by a factor of Q reduces the computational complexity of the proposed DFT-based delay estimation by Q times.
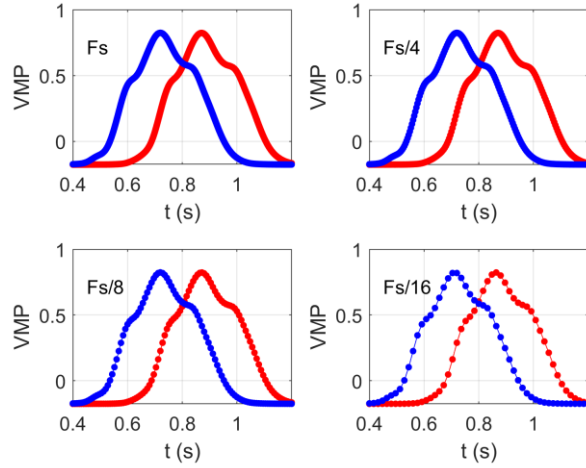
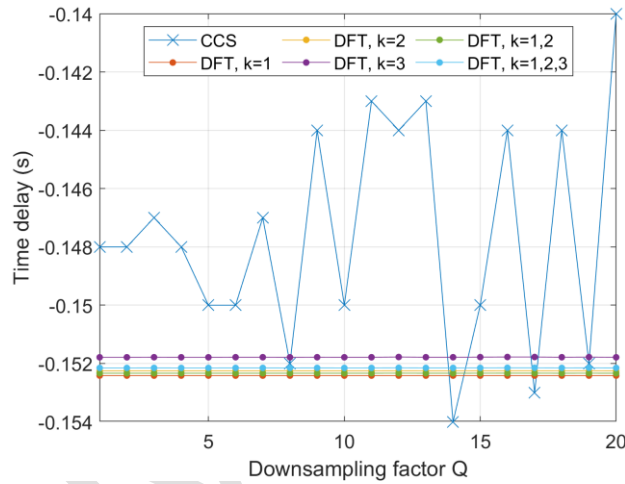Fig. 13. Downsampled VMPs signals $p_1[n]$ and $p_3[n]$.

Fig. 14. Time delay estimation results for downsampled signals for CCS-based and DFT-based algorithms. The VMPs for downsampling factors Q equal 4, 8, and 16 are depicted in Fig. 13.

4.5. Noise immunity

Figure 15 presents the mean value and std of shift estimation errors for n_s=-150 and both VMPs disturbed by *additive white Gaussian noise* (AWGN) across a range of *signal-to-noise ratios* (SNR) from 0 dB to 60 dB. The mean value and the std of the delay estimation error were computed from 10^6 signal realizations for each SNR. It is observed in Fig. 14 that the CCS-based estimation is biased, as the mean error is over 3, which is consistent with the results in Figs. 11, 12. The bias of the estimation based on the DFT is close to zero. The standard deviation of all DFT-based methods is also lower than the standard deviation of the CCS-based estimation.
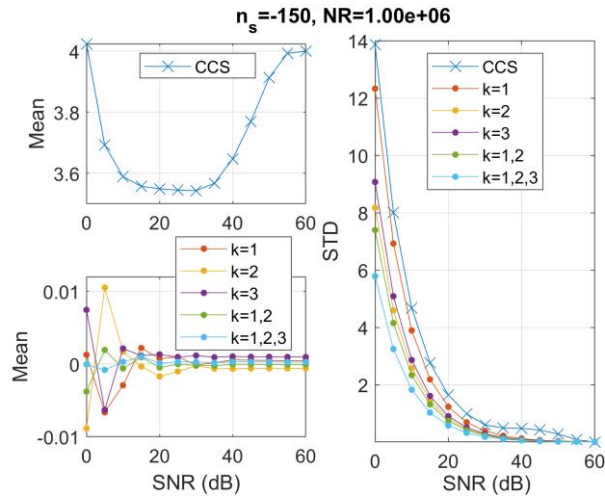
Fig. 15. Mean value and std of shift estimation error for CCS-based and DFT-based algorithms for n_s=-150 and AWGN, *NR* denotes the number test signal of realizations.

Figure 14 illustrates the superior performance of the proposed DFT-based delay estimation application compared to the CCS-based estimation for noisy signals. The best results were obtained for the delay calculated using (9) and slightly worse results were obtained by using (8).

Noise immunity is an important general property of any estimation method, however in the presented MFIM system, wide-band noise is suppressed through signal preprocessing. The perfectly flat-top filters used for signal demodulation [1] have a very narrow passband, which effectively suppresses broadband disturbances such as white noise. Downsampling from 400 kHz to 1 kHz involves the use of an additional lowpass filter what further reduces wideband noise.

5. Conclusions

The paper presents a DFT-based algorithm for estimating the fractional shift between two VMPs of a passing vehicle, which is then used to determine its speed. The computational properties of the algorithm are demonstrated using real-world VMPs obtained from a fully operational MFIM system located at the internal road of AGH University campus. The DFT-based time delay estimation has the advantage of fractional estimation, which occurs between sampling times. This is very convenient because downsampling VMP signals reduces the computational complexity of shift estimation, as well as makes data management (*i.e.* transmission and storage) of downsampled VMPs more efficient.

The paper presents a proof of concept, and long-term observations will be conducted next. The developed MFIM system is planned to be used on a national road with an estimated number of a few thousand vehicles passing per day. A single passage produces 6 VMPs due to resistive and reactive components, both computed for each of the three measurement frequencies. Thus, the MFIM system will face a big data problem with computing, storing, and transmitting all VMPs. In this respect, a low sampling frequency is strongly preferred. The proposed DFT-based estimation method can operate effectively with low sampling frequencies while maintaining high accuracy, unlike the standard CCS-based estimation method, which necessitates high sampling frequencies.

In a future large-scale, long-term research study, the DFT-based algorithm will initially operate concurrently with the CCS-based algorithm in our MFIM system for additional validation and comparison between the two. As the two algorithms operate based on different principles, *i.e.*, in the time and frequency domains, they can both be utilized for data fusion in the case of significantly disturbed VMPs. It is expected that the disturbance will affect each

method differently. Finally, the decision will be made on whether the DFT-based computations will replace the CCS in the MFIM system or if both will work in conjunction.

Although the presentation focuses on inductive-loop technology and vehicle VMP, we anticipate that the described DFT-based fractional time delay estimation is also applicable to other types of sensors used in road traffic measurements, and generally to any system requiring time shift estimation between short-duration, low-oscillation, impulse-like signals. The substitution of the cross-correlation with the proposed DFT-based shift estimation in a road traffic measurement system can lead to better results in the sense of higher accuracy, thanks to fractional shift estimation, and also lower computational complexity.

Acknowledgements

References

[1] Marszalek, Z., & Duda, K. (2020). Multifrequency vector measurement system for reliable vehicle magnetic profile assessment, *Sensors*, *20*(17), 1–15. https://doi.org/10.3390/s20174933

[2] Marszalek, Z., Gawedzki, W., & Duda, K. (2021). A reliable moving vehicle axle-to-axle distance measurement system based on multi-frequency impedance measurement of a slim inductive-loop sensor. *Measurement*, *169*(108525), 1–9, https://doi.org/10.1016/j.measurement.2020.108525

[3] Marszałek, Z., Duda, K., Piwowar, P., Stencel, M., Żegleń, T., & Izydorczyk, J. (2023). Load estimation of moving passenger cars using inductive-loop technology. *Sensors*, *23*(4), 1–19. https://doi.org/10.3390/s23042063

[4] Sheykhmousa, M., Mahdianpari, M., Ghanbari, H., Mohammadimanesh, F., Ghamisi, P., & Homayouni, S. (2020). Support vector machine versus random forest for remote sensing image classification: a meta-analysis and systematic review. *IEEE Journal of Selected Topics in Applied Earth Observations and Remote Sensing*, *13*, 6308–6325. https://doi.org/10.1109/JSTARS.2020.3026724

[5] Jeng, S.T.C., & Ritchie, S.G. (2008). Real-time vehicle classification using inductive loop signature data. *Transportation Research Record: Journal of the Transportation Research Board*, *2086*(1), 8–22. https://doi.org/10.3141/2086-02

[6] Ki, Y.K., Baik, & D.K. (2006). Vehicle-classification algorithm for single loop detectors using neural networks. *IEEE Transactions on Vehicular Technology*, *55*, 1704–1711. https://doi.org/10.1109/TVT.2006.883726

[7] Mosa, A.H., Kyamakya, K., Junghans, R., Ali, M., Machot, F.A., & Gutmann, M. (2016). Soft radial basis cellular neural network (SRB-CNN) based robust low-cost truck detection using a single presence detection sensor. *Transportation Research Part C: Emerging Technologies*, *73*, 105–127. https://doi.org/10.1016/j.trc.2016.10.016

[8] Sassella, A., Abbracciavento, F., Formentin, S., Bianchessi, A. G., & Savaresi, S. M. (2023, May). On queue length estimation in urban traffic intersections via inductive loops. *In 2023 American Control Conference (ACC)* (pp. 1135-1140). IEEE. https://doi.org/10.23919/ACC55779.2023.10156258

[9] Taghvaeeyan, S., & Rajamani, R. (2014). Portable roadside sensors for vehicle counting classification and speed measurement. *IEEE Transactions on Intelligent Transportation Systems*, *15*(1), 73–83. https://doi.org/10.1109/TITS.2013.2273876

[10] Balid, W., Tafish, H., & Refai, H.H. (2018). Intelligent vehicle counting and classification sensor for real-time traffic surveillance. *IEEE Transactions on Intelligent Transportation Systems*, *19*(6), 1784–1794. https://doi.org/10.1109/TITS.2017.2741507

[11] Markevicius, V., Navikas, D., Idzkowski, A., Valinevicius, A., Zilys, M., Janeliauskas, A., Walendziuk, W., & Andriukaitis, D. (2021). An effective method of vehicle speed evaluation in systems using anisotropic magneto-resistive sensors. *IEEE Intelligent Transportation Systems Magazine*, *13*(2), 142–151. https://doi.org/10.1109/MITS.2018.2889693

[12] Miklusis, D., Markevicius, V., Navikas, D., Cepenas, M., Balamutas, J., Valinevicius, A., Zilys, M., Cuinas, I., Klimenta, D., & Andriukaitis, D. (2021). Research of distorted vehicle magnetic signatures recognitions, for length estimation in real traffic conditions. *Sensors*, *21*(23), 7872. https://doi.org/10.3390/s21237872

[13] Yao R., & Uchiyama T. (2024). Analysis of magnetic signatures for vehicle detection using dual-axis magneto-impedance sensors. *IEEE Sensors Journal*, *24*(6), 8721–8730. https://doi.org/10.1109/JSEN.2024.3357852

[14] Zhang, C., Shen, S., Huang, H., & Wang, L. (2021). Estimation of the vehicle speed using cross-correlation algorithms and mems wireless sensors. *Sensors*, *21*(5), 1721. https://doi.org/10.3390/s21051721

[15] U. D. of Transportation. (2016). *Traffic monitoring guide*. Federal Highway Administration (FHWA). https://www.fhwa.dot.gov/policyinformation/tmguide/tmg_fhwa_pl_17_003.pdf

[16] Gholamhosseinian, A., & Seitz, J. (2021). Vehicle Classification in Intelligent Transport Systems: An Overview, Methods and Software Perspective. *IEEE Open Journal of Intelligent Transportation Systems*, *2*, 173–194. https://doi.org/10.1109/ojits.2021.3096756

[17] Maczyński, A., Brzozowski, K., & Ryguła, A. (2021). Analysis and Prediction of Vehicles Speed in Free-Flow Traffic. *Transport and Telecommunication Journal*, *22*(3), 266–277. https://doi.org/10.2478/ttj-2021-0020

[18] Knapp, C., & Carter, G. (1976). The generalized correlation method for estimation of time delay. *IEEE Transactions on Acoustics, Speech, and Signal Processing*, *24*(4), 320–327. https://doi.org/10.1109/tassp.1976.1162830

[19] Carter, G. C. (1987). Coherence and time delay estimation. *Proceedings of the IEEE*, *75*(2), 236–255. https://doi.org/10.1109/proc.1987.13723

[20] Chen, J., Benesty, J., & Huang, Y. (Arden). (2005). Performance of GCC- and AMDF-Based Time-Delay Estimation in Practical Reverberant Environments. *EURASIP Journal on Advances in Signal Processing*, *2005*(1). https://doi.org/10.1155/asp.2005.25

[21] Shaswary, E., Xu, Y., & Tavakkoli, J. (2016). Performance study of a new time-delay estimation algorithm in ultrasonic echo signals and ultrasound elastography. *Ultrasonics*, *69*, 11–18. https://doi.org/10.1016/j.ultras.2016.03.002

[22] Velickovic, Z. S., & Pavlovic, V. D. (2013). The Performance of the Modified GCC Technique for Differential Time Delay Estimation in the Cooperative Sensor Network. *Electronics and Electrical Engineering*, *19*(8). https://doi.org/10.5755/j01.eee.19.8.2445

[23] Xiaoming Lai, & Torp, H. (1999). Interpolation methods for time-delay estimation using cross-correlation method for blood velocity measurement. *IEEE Transactions on Ultrasonics, Ferroelectrics and Frequency Control*, *46*(2), 277–290. https://doi.org/10.1109/58.753016

[24] Gontarz, S., Szulim, P., Seńko, J., & Dybała, J. (2015). Use of magnetic monitoring of vehicles for proactive strategy development. *Transportation Research Part C: Emerging Technologies*, *52*, 102–115. https://doi.org/10.1016/j.trc.2014.12.007

[25] Shimamura, T., & Kobayashi, H. (2001). Weighted autocorrelation for pitch extraction of noisy speech. *IEEE Transactions on Speech and Audio Processing*, *9*(7), 727–730. https://doi.org/10.1109/89.952490

[26] Kim, D.-H., Choi, K.-H., Li, K.-J., & Lee, Y.-S. (2014). Performance of vehicle speed estimation using wireless sensor networks: a region-based approach. *The Journal of Supercomputing*, *71*(6), 2101–2120. https://doi.org/10.1007/s11227-014-1306-7

[27] Zhu, H., & Yu, F. (2016). A Cross-Correlation Technique for Vehicle Detections in Wireless Magnetic Sensor Network. *IEEE Sensors Journal*, *16*(11), 4484–4494. https://doi.org/10.1109/jsen.2016.2523601

[28] Liu, W., Li, L., Li, L., Jiao, H., Qu, J., & Sun, G. (2024). Velocity Estimation of Underwater Vehicle Based on Abnormal Magnetic Field Waveform. *IEEE Sensors Journal*, *24*(1), 367–376. https://doi.org/10.1109/jsen.2023.3324431

[29] Wang, Z., Song, R., Chen, W., Wang, J., Wang, P., Ming, Z., & Zhang, Z. (2024). A general method for trace substance detection based on cross-correlation theory. *Sensors and Actuators B: Chemical*, *415*, 135987. https://doi.org/10.1016/j.snb.2024.135987

[30] Duda, K., Zielinski, T. P., & Barczentewicz, S. H. (2016). Perfectly Flat-Top and Equiripple Flat-Top Cosine Windows. *IEEE Transactions on Instrumentation and Measurement*, *65*(7), 1558–1567. https://doi.org/10.1109/tim.2016.2534398

[31] Oppenheim, A. V., Schafer, R. W., & Buck, J. R. (1999). *Discrete-Time Signal Processing, 2nd Edition*. Prentice-Hall.

[32] Harris, F. J. (1978). On the use of windows for harmonic analysis with the discrete Fourier transform. *Proceedings of the IEEE*, *66*(1), 51–83. https://doi.org/10.1109/proc.1978.10837

[33] Blok, M., & Sac, M. (2014). Variable Fractional Delay Filter Design Using a Symmetric Window. *Circuits, Systems, and Signal Processing*, *33*(10), 3223–3250. https://doi.org/10.1007/s00034-014-9803-8

Krzysztof Duda received the M.S. degree in automatics and metrology and the Ph.D. degree in electronics from the AGH University of Krakow, Poland, in 1998 and 2002, respectively.

He has been with the Department of Measurement and Electronics, AGH University, where, from 2002 to 2019, he was an Assistant Professor, and since 2019, he has been a Professor. His current research interests include the development and applications of digital signal processing and analysis.

Zbigniew Marszalek received the M.S degree in automatic and metrology and the Ph.D. degree in electrical engineering from the AGH University of Krakow, Poland, in 2008 and 2014, respectively.

He has been with the Department of Measurement and Electronics, AGH University, where, since 2014 he has been Assistant Professor. His current research interests include the ARM Linux embedded systems, vehicle axle detection based on multi-frequency inductive-loop detector technology, and vehicle in motion parameters measurement and classification systems.